Fully polarimetric high-resolution airborne SAR image change detection with morphological component analysis

Mendez Dominguez, Elias; Henke, Daniel; Small, David; Meier, Erich

Abstract: Change detection for high resolution Synthetic Aperture Radar (SAR) imagery requires advanced denoising mechanisms to preserve details and minimize speckle. In this work, we propose a change detector based on a Morphological Component Analysis (MCA) of the scattering mechanisms provided with fully polarimetric data sets. With MCA, the power of each scattering mechanism is decomposed into diverse image features. By introducing a priori knowledge of the content of the scenes, and exploiting both the scattering mechanisms and their corresponding shapes, we can significantly improve performance, with fewer false alarms introduced by clutter, focusing errors, and inconsistent acquisition geometries.

DOI: https://doi.org/10.1117/12.2194780

Fully Polarimetric High Resolution Airborne SAR Image Change Detection with Morphological Component Analysis

E. Mendez Dominguez*, D. Henke, D. Small, E. Meier
Remote Sensing Laboratories RSL, Department of Geography, University of Zurich,
Winterthurerstrasse 190, CH-8057, Switzerland

ABSTRACT

Change detection for high resolution Synthetic Aperture Radar (SAR) imagery requires advanced denoising mechanisms to preserve details and minimize speckle. In this work, we propose a change detector based on a Morphological Component Analysis (MCA) of the scattering mechanisms provided with fully polarimetric data sets. With MCA, the power of each scattering mechanism is decomposed into diverse image features. By introducing *a priori* knowledge of the content of the scenes, and exploiting both the scattering mechanisms and their corresponding shapes, we can significantly improve performance, with fewer false alarms introduced by clutter, focusing errors, and inconsistent acquisition geometries.

1. INTRODUCTION

Image change detection is a technique that captures the changes occurring in multiple images acquired over the same area at different times. The procedure interrogates a test image with respect to a reference image to obtain a change map. This application is useful for observation of environmental and human activity, risk management, agricultural surveys, and urban studies. Some of these applications require collecting data independently of weather and daylight conditions. For this reason, SAR offers a good alternative to optical sensors providing time series data with both fine temporal and spatial resolutions. Previous studies [1], [2], [3] showed great potential for SAR-based image change detection. Nonetheless, the inherent complexity of SAR data imposes multiple challenges such as noise suppression, registration noise and calibration errors that still need to be investigated [4].

Most SAR-based change detectors are designed to mitigate errors caused by the presence of noise. Multichannel data sets (polarimetric, interferometric) offer a good solution to alleviate this source of error, yielding improved results compared to single channel SAR imagery at the cost of increasing the data input. Much effort has been devoted to validate and study multiple dissimilarity functions suitable for multichannel SAR imagery. The approach described in [5], introduces the log-likelihood test assuming that the coherence matrices follow a complex Wishart distribution, showing a good detection performance in forested areas. The work presented in [6] introduces an inter-comparison of diverse statistical- and non-statistical-based approaches to extract changes from polarimetric data sets using simulated scenarios. The authors concluded that the assumption of the probability distribution function impacts the performance of the change detector, introducing a more difficult characterization of their detection capabilities. The method described in [7] exploits the coherence in combination with a log-likelihood test utilizing polarimetric and interferometric SAR data (PolInSAR) to detect changes produced by vehicle and foot tracks. In addition to statistics-based approaches, other dissimilarity functions suitable for polarimetric data sets were summarized in [8], where an inter-comparison of their performance was also provided.

In this context, less work has been devoted to study other aspects introduced by multichannel data sets, such as exploitation of the polarimetric information, shape, or texture analysis. Our work is based on the method described in [9], where an enhancement technique of the curvelet coefficients of the power of the scattering mechanisms is utilized to highlight changes related to man-made objects. To overcome some limitations, in particular with high resolution airborne SAR imagery, we exploit shape-based decomposition techniques combined with polarimetric layers to provide physically meaningful features to the change detector. In this manner, we exploit six image features (three scattering mechanisms decomposed in two shapes) to remove false alarms introduced by clutter, diverse focusing errors (sidelobes, moving targets…), and differences caused by non-uniform acquisition geometries, e.g. migration of the Point Spread Functions (PSFs) of a given target to different image pixels.

Image and Signal Processing for Remote Sensing XXI, edited by Lorenzo Bruzzone, Proc. of SPIE
Vol. 9643, 964312 · © 2015 SPIE · CCC code: 0277-786X/15/$18 · doi: 10.1117/12.2194780

This paper is organized as follows: Section 2 introduces the design of the change detector including the data preparation, polarimetric decomposition and image feature extraction. The steps required handling the false alarms induced by clutter, focusing errors and difference between acquisition geometries are also described. Section 3 illustrates the results obtained with real multitemporal SAR data, presenting the performance of the approach in typical urban scenarios. Section 4 concludes with a discussion of the results and reports conclusions.

2. METHOD

Data and Test Site

The data sets were acquired with DLR's F-SAR sensor [10] over Memmingen (Germany) and Oensingen (Switzerland). The SAR images were recorded at X-band in fully polarimetric mode with a linear stripmap configuration. The characteristics of the images and their acquisition geometries are listed in Table 1, reflecting typical variations in airborne SAR. The passes acquired in Oensingen are geometrically calibrated by using deployed corner reflectors along the illuminated area, yielding residual range and azimuth offsets well below 2 centimetres. For the passes recorded in Memmingen, the images were co-registered with the method described in [11] to alleviate possible registration noise. The RAW data was processed with a matched filter in range, and an interpolated matched filter in azimuth (Time Domain Back-Projection). To attain the highest possible resolution, we utilized single-look processing mode with no windowing for sidelobe suppression.

Table 1. F-SAR X-band Data Sets.

Image	Location	Slant Range Resolution [m]	Azimuth Resolution [m]	Incidence Angle [°]	Flight Heading [°]	Date	Δt
MEM1	Memmingen	0.2	0.13	52°	280°	17/10/13 12:13:09	8d
MEM2	Memmingen	0.2	0.13	52°	274°	25/10/13 12:48:32	
OEN1	Oensingen	0.5	0.15	47°	45°	16/06/10 09:23:00	43m
OEN2	Oensingen	0.5	0.15	51°	45°	16/06/10 10:06:16	

Data Preparation

The SAR images were radiometrically calibrated relatively after removing the range spreading losses and the influence of the antennae patterns in transmission and reception. To compensate for cross talk and channel imbalance [12], we performed polarimetric calibration with the iterative method described in [13]. Finally, the power of the scattering mechanisms (single-bounce, double-bounce and volume scattering) is calculated for each data set with a suitable decomposition (i.e. the Pauli decomposition as described in [14]). To detect changes at the resolution of the original SAR images we applied the coherent Pauli decomposition. If an incoherent decomposition is desired, the size of the sliding window must be set to one pixel. Otherwise, the resolution degradation is proportional to the sliding window size in use. The power of the scattering mechanisms is computed for each data set, and color-coded in an RGB composite.

As a first attempt to mitigate the errors induced by noise, we applied a preliminary noise treatment to each RGB image. To avoid skewing of the polarimetric information, we performed an advanced color image denoising with Color Block-Matching 3-D (C-BM3D) described in [15].

MCA with polarimetric data sets

With the previous RGB composites of each data set, we obtained three physically meaningful image features. To further exploit this information and improve the performance of the change detector, we utilized the shape of the different image features of the power of each scattering mechanism. Assuming that the log-transform power of a certain scattering mechanism, x, can be expressed as:

$$x=y+\varepsilon \quad (1)$$

where y is the noise-free power of the scattering mechanism, and ε is the remaining additive Gaussian noise (with zero mean and standard deviation σ_ε). We decompose x into different shapes, focusing on a decompose-denoise method that works in a transformed domain using a multiresolution decomposition and shrinking rules [16]. The design of the method is based on the compressed sensing theorem [17], where we assume that a certain morphological transform is able to represent the data in a sparse form. For instance, wavelets provide reliable sparse representation of smooth/uniform areas and point-like targets, but fail to represent other types of image content such as lines or edges. However, these types of shapes are well represented by curvelets [17],[18]. For this reason, it is desirable to account for the different geometric features found in high resolution SAR imagery, exploiting the advantages of different morphological transforms when used in combination [17]. Considering typical shapes found in high resolution SAR imagery, the power of a certain scattering mechanism x can be expressed as the linear combination of the coefficients of its wavelet and curvelet domain, when x is corrupted with additive noise ε:

$$x = \Psi_{swt}\alpha_{swt} + \Psi_{curv}\alpha_{curv} + \varepsilon \quad (2)$$

where α_{swt} and α_{curv} are the matrices of coefficients of y in the transformed domain Ψ_{swt} and Ψ_{curv} respectively. To solve (2) we apply a morphological component analysis to restrict the space of possible solutions or candidates by computing:

$$\min_{\alpha_{swt},\alpha_{curv}} \left(\|\alpha_{swt}\|_1^1 + \|\alpha_{curv}\|_1^1\right) \text{ s.t. } \|x - \Psi_{swt}\alpha_{swt} - \Psi_{curv}\alpha_{curv}\|_2 \leq \sigma \quad (3)$$

To solve (3), we need to find the set of coefficients α_{swt} and α_{curv} of the wavelet and curvelet domain that have the minimum ℓ_1 norm (which produces a more sparse representation) with the minimum reconstruction error σ (fidelity to data). If we fix all the coefficients α_l but α_k, we can find a solution by soft-thresholding the coefficients of the marginal residuals r_k, computed as:

$$r_k = x - \sum_{l \neq k} \Psi_l \alpha_l \quad (4)$$

The soft-thresholding shrinking rule is defined as:

$$\text{SoftThresh}(X,T) = \text{sign}(X)(|X| - T) \quad (5)$$

where X is a generic real variable and the threshold T is computed via:

$$T = a_0 \cdot \text{median}(|w_3 - \text{median}(w_3)|)/c_0 \quad (6)$$

with w_3 being the coefficients of the diagonal subband of the Haar wavelet of the input x obtained at the first resolution scale, c_0=0.6745 [17][18]. The parameter a_0 introduces a smoothing factor depending on the noise level still present in the input. In this work, we utilize the standardized a_0=1.5 for soft-thresholding as described in [17].

The evaluation of (4) is the basis of the iterative procedure of MCA. To evaluate the performance of the method at each iteration we use the adaptive MCA - Mean of Maxima (MCA-MOM) described in [19]. This method yields better performance when the components provide a different directional analysis, and ensures that each transform gets at least one assigned component [17]. However, due to mathematical limitations, all targets are expressed as a combination of all the transforms involved, and thus a "perfect" separation of shapes cannot be guaranteed. After reaching a stopping criteria, the input is decomposed into its wavelet and curvelet components, so that the summation of both leads to a denoised version of the input image that depends on the parameter a_0.

Change Detection with polarimetric layers and MCA

To extract changes we first calculated a Difference Image (DI) by subtracting the power of the scattering mechanisms of the reference and test data sets, utilizing the C-BM3D denoised RGB composites. The result of this operation yields three difference images, referred to as DI_x with x={even-bounce, odd-bounce, volume}. Subsequently, to solve equation (2), each DI_x is decomposed into its wavelet and curvelet components with MCA-MOM. The final set of image features is referred to as $DI_{x,y}$, with y={wavelet, curvelet}. To obtain the change maps that correspond to each feature $DI_{x,y}$, a thresholding or classification technique is required. In this work, we performed manual thresholding with a fixed threshold T_1 for the entire set $DI_{x,y}$. Better results might be achieved when using separate thresholds for the different image features. After thresholding, we obtained a set of six change maps, $CM_{x,y}$, that could be combined to retain changes of interest while discarding the rest. The combination of the change maps is performed at the feature level, using

logical operators such as AND, OR or XOR, depending on the *a priori* knowledge gathered from the scenes. This demands human interaction: the scattering mechanisms characterizing the different targets (e.g. cars) depend on the aspect angles and can vary significantly. Considering parking lots, where cars are oriented in parallel, we assumed that the dominant scattering mechanisms stayed constant for all cars present in that specific scene. In this manner, the dominant scattering mechanism has to be identified manually before combining the different change maps. Nonetheless, the aspect angle of the different targets can be derived automatically using either the parameters involved in the acquisition geometry and the image content, or exploiting the orientation angle extracted from the polarimetric information [14]. However, that topic is beyond the scope of this paper.

3. RESULTS

We apply the method described in section 2 on data from two test sites: Memmingen, Germany and Oensingen, Switzerland. In the following, we present the results for each test site using (1) the color-coded Pauli decomposition[1] of the two acquisitions, (2) the RGB composite of the reference and test images (RGB-RT), and (3) the change maps obtained with MCA. For the RGB-RT (2), the likelihood of being a change *from the image space point of view* increases with increasing red (disappearing target) and green (appearing target) colors, whereas yellow indicates a low probability of change. The purpose of the RGB-RT is not to define a "ground truth", but to give the reader an indication of potential changes on the ground. The change maps (3) are overlaid on top of the span of the reference image. The maps contain two classes: pixels marked in green/red indicate when a target entered/left the scene.

Test Site: Memmingen

The area of interest is located at the Ällgau airport in Memmingen. In this test site, the changes occurred due to the movement of cars, a civilian aircraft and some luggage transporters. Figure 1 illustrates the denoised RGB composites of the Pauli decomposition of the two corresponding data sets (see Table 1).

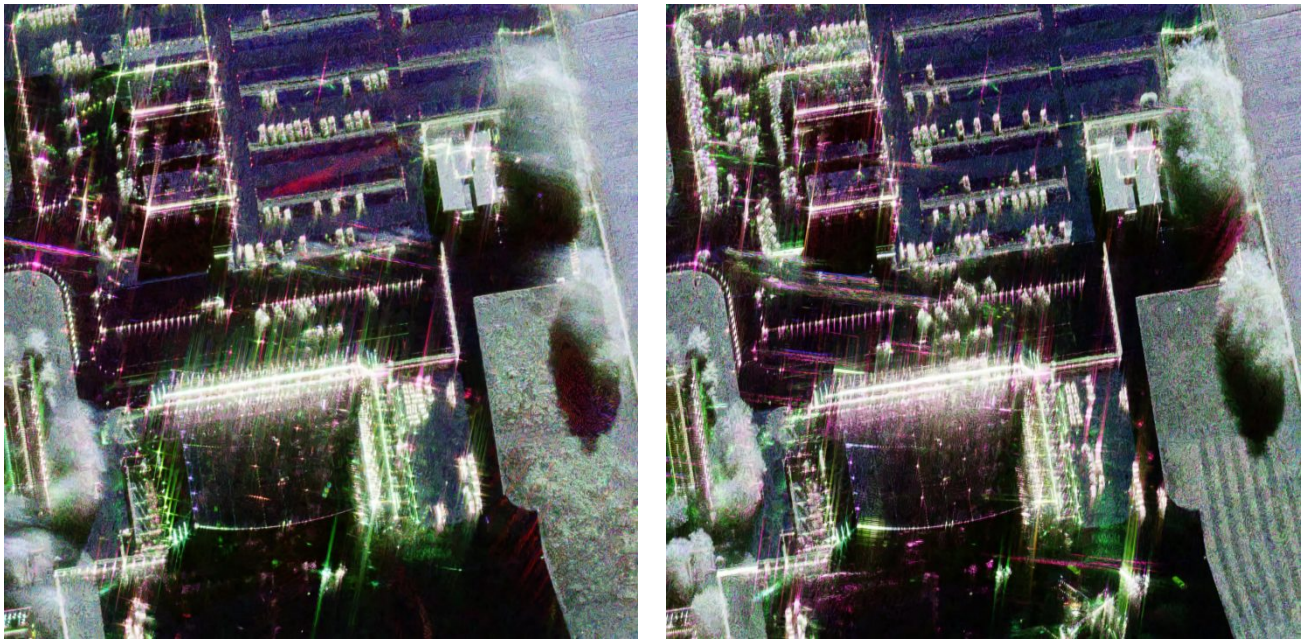

Figure 1. Color-coded Pauli decomposition for F-SAR X-band MEM1 (left) and MEM2 (right).

[1] The power of the scattering mechanism is coded in an RGB composite, where the red channel corresponds to the power of the even-bounce, the green channel corresponds mainly to the power of the volume scattering, and the blue channel represents the power of the odd-bounce mechanism.

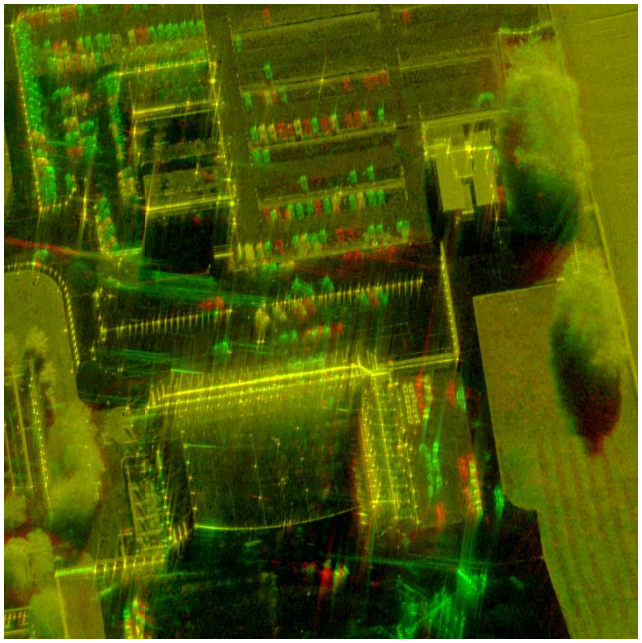

(a) RGB-RT[2]: R= total scatter power of the reference image; G= total scatter power of the test image; B=zero image.

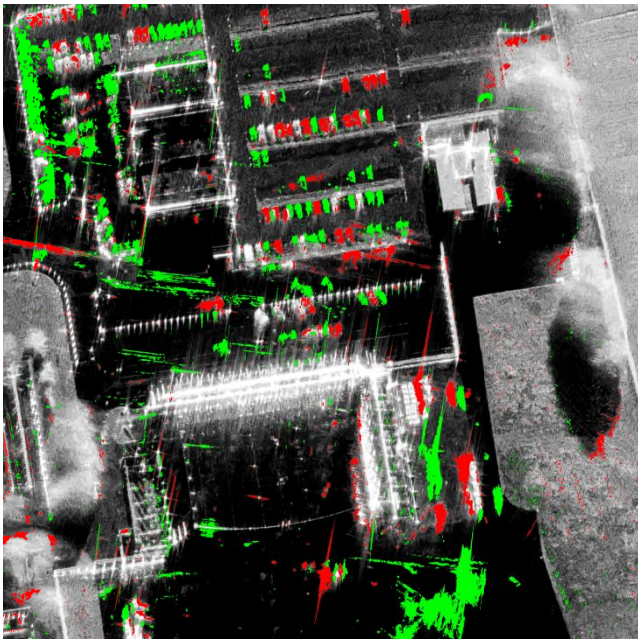

(b) Change map extracted with all scattering mechanisms and all their corresponding shapes.

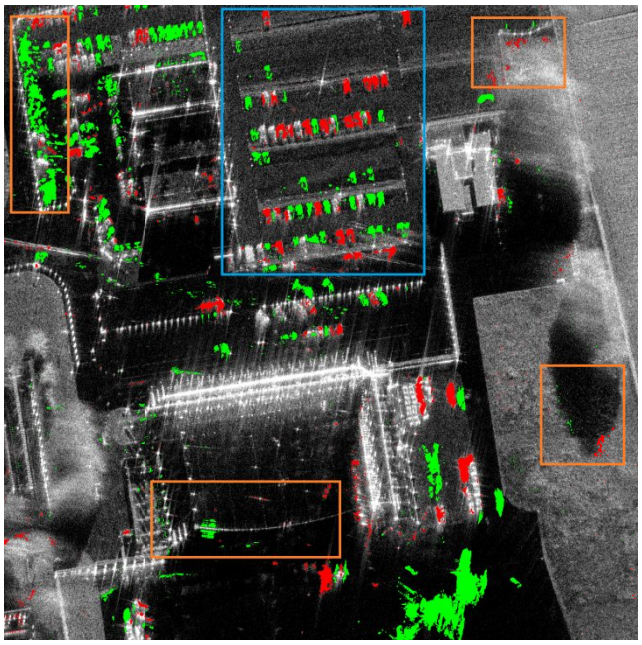

(c) Change map extracted with the wavelet component of the volume scattering mechanism.

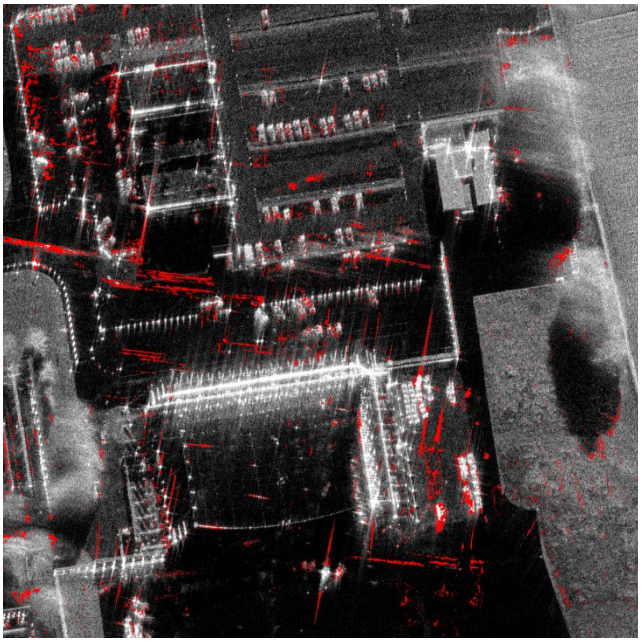

(d) Differences of the change maps given in (b) and (c).

Figure 2. Results of the change detector based on polarimetric layers and shape information (MEM1-MEM2).

Figure 2(a) shows the RGB-RT of the scene. Figure 2(b) illustrates the change map computed with all the scattering mechanisms and shapes; i.e. $\vee CM_{x,y}, \forall\{x,y\}$. In this case, several side-lobes, clutter, and moving targets were wrongly detected as changes. However, the most likely real changes on the ground can be characterized by exploiting the

[2] This RGB composite is produced with the span (the total scattered power) of the reference image in the red channel and the span of the test image in the green channel. The blue channel is the null matrix.

difference of the power of the volume scattering mechanism (green channel), as one can observe in Figure 1. Considering the shape information, the curvelet component of each mechanism can be associated to the false alarms caused by side-lobes, moving targets and clutter. To validate these assumptions, Figure 2(c) shows the change map obtained with the wavelet component of the volume scattering mechanism only; i.e $CM_{volume,wavelet}$. Figure 2(d) shows the removed false alarms indicated by a red mask overlaid on the span of the reference. Additionally, in Figure 2(c) we marked areas of special interest with rectangles. In the blue rectangle of a parking lot, each individual car can be separated and identified. In contrast, the changes produced by the cars inside the orange rectangle on the top-left side of the image cannot be individually identified. Furthermore, some errors are due to movement of the trees, shadowing, and the change of the scattering mechanisms of some objects of the rooftop of the terminal. These were not successfully cancelled (see the orange rectangles on the right and bottom part of the image). We will comment on the reasons in the discussion section.

Test Site: Oensingen

This test site is located in the commercial area of Oensingen. In this test site, most changes on the ground occurred most probably due to movement of cars or trucks. Figure 3 shows the denoised RGB composites of the Pauli decomposition for the two corresponding data sets (see Table 1). The RGB-RT is shown in Figure 4(a). The areas where changes most likely occurred on the ground are indicated by a blue rectangle, and serve as a "ground truth" indicator.

Figure 4(b) shows the change map computed with all the scattering mechanisms and shapes using $\vee CM_{x,y}, \forall\{x,y\}$. However, in this case the migration of the PSFs (due to slight differences between the acquisition geometries), and clutter are detected incorrectly as changes. By interpreting the RGB composites from Figure 3, the walls of the buildings are characterized with the power of the even-bounce mechanism (red channel) and its curvelet component. However, the clutter area is characterized by a mixture of both even and odd bounce (red and blue channels) with a shape factor possibly attached to the wavelet domain. In addition, the cars do not show the presence of a clearly dominant mechanism, but their point-like shape indicates that the wavelet component is again more suitable to detect the changes produced by these targets. Bearing the previous considerations in mind, we wish to retain the changes commonly detected with all scattering mechanisms attached to the wavelet domain; i.e. $\wedge CM_{x,wavelet}, \forall\{x\}$. In this manner, the false alarms produced by clutter and the walls of the buildings can be successfully suppressed as one observe in Figure 4(c). The remaining errors are indicated by orange rectangles. Reasons for these false alarms are discussed in section 4. Finally, and for comparison purposes, Figure 4(d) illustrates in red the cancelled false alarms.

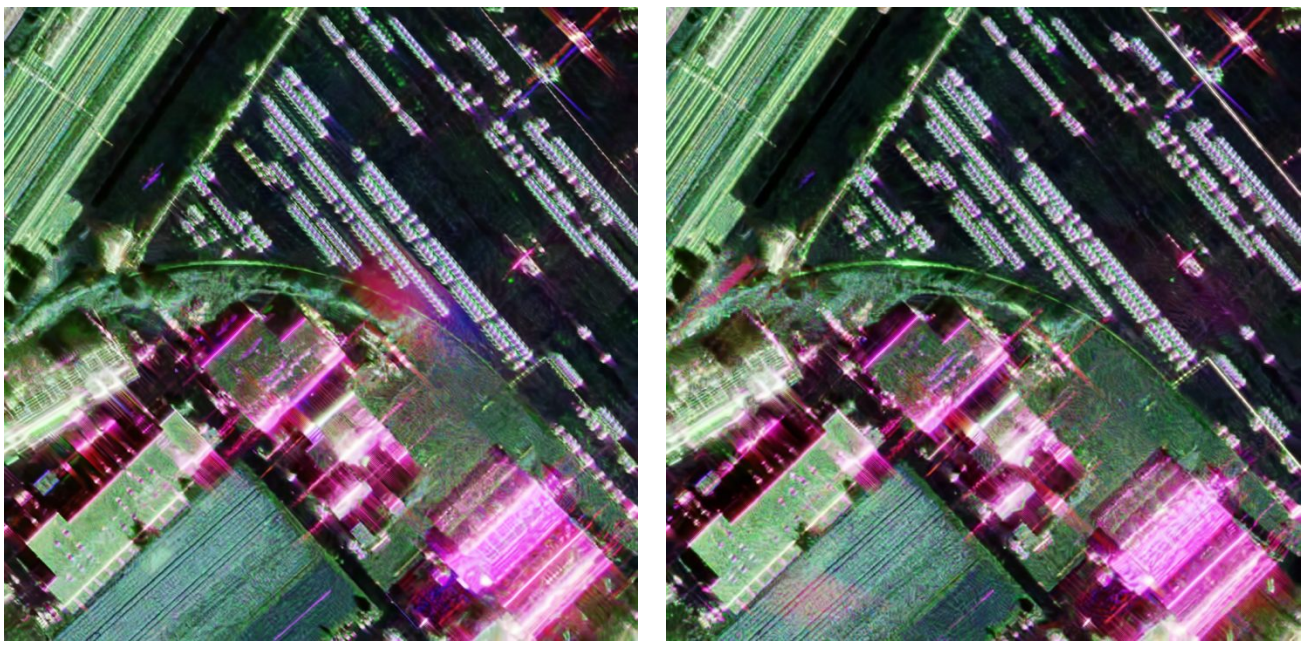

Figure 3. Color-coded Pauli decomposition for OEN1 (left) and OEN2 (right).

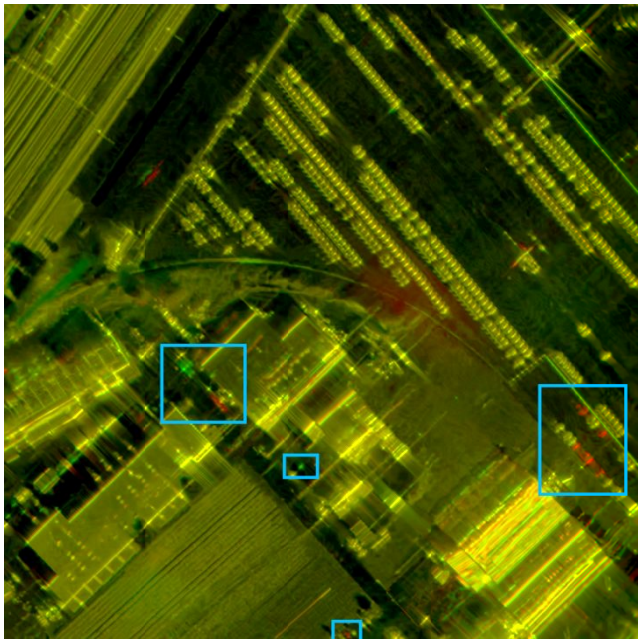

(a) RGB-RT: R= total scatter power of the reference image; G= total scatter power of the test image; B=zero image.

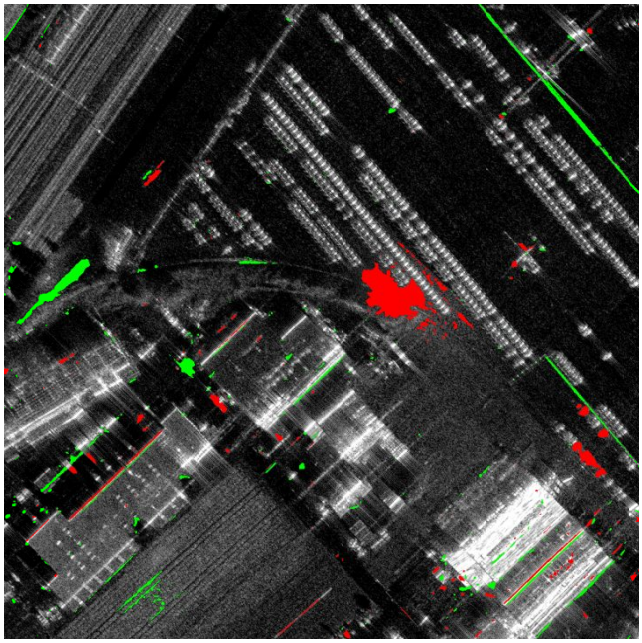

(b) Change map extracted with all scattering mechanisms and all their corresponding shapes.

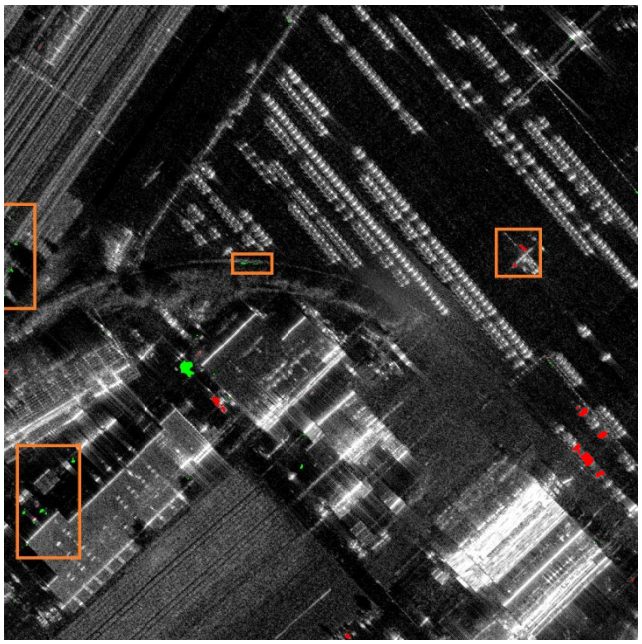

(c) Change map extracted with the changes detected in common with the wavelet component of all scattering mechanisms.

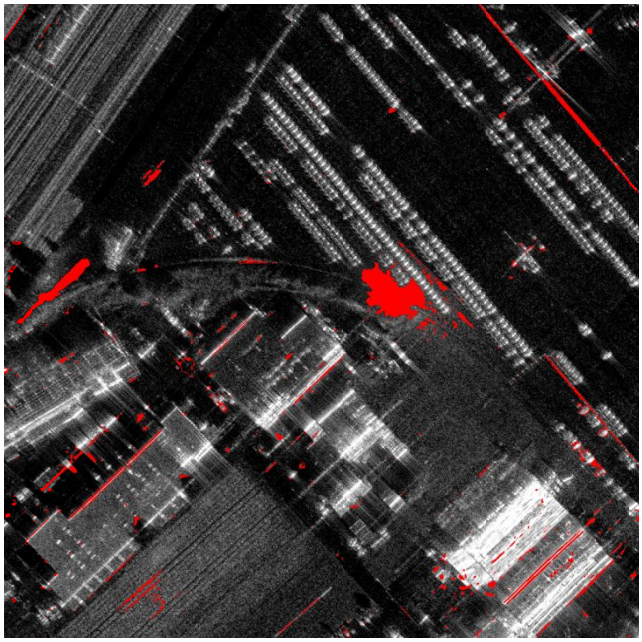

(d) Differences of the change maps shown in (b) and (c).

Figure 4. Results of the change detector based on polarimetric layers and shape information (OEN1-OEN2).

4. DISCUSSION

Analysis of the Results

The algorithm was evaluated concentrating on two different areas of interest. The changes that occurred in the first test site (Memmingen) were dominated by point-like shapes produced by the movement of man-made objects, assuming quasi-identical acquisition geometries. From Figure 2, and considering noise as the only source of error, the change maps did not show significant false alarms in uniform areas. The combination of C-BM3D and the inherited shape-properties provided by MCA, generally outperformed the outputs obtained by classical noise suppression methods. The usage of the wavelet component of the volume scattering provided a good solution that considered the available image features. The reasons are: (1) most side-lobes and moving cars were attached to the curvelet component, independently of the scattering mechanism; (2) the false alarms induced by clutter could be suppressed with the even- and odd-bounce mechanism independently of the shape of the changes; and (3) the changes produced by the movement of the cars, the aircraft and the luggage transporters could be detected with the difference of the power of the volume scattering.

Inspecting Figure 2 (c), we observed several false alarms still remaining in the change map. One reason was the slight difference in heading of the flight paths introducing a displacement of the shadows originated from elevated targets, such as trees. In these areas, small patches of false alarms occur, as indicated by orange rectangles on the right side in Figure 2(c). In shadowed areas, the scattering mechanisms cannot be exploited and the shape of the changes originated after subtraction are unpredictable.

Different weather conditions (windy/wet versus calm/dry) occurred during MEM 1 and MEM 2 respectively, introducing false alarms due to defocusing of the (moving/static) trees. In this situation, the change map extracted from the power of the volume scattering could not be exploited, as natural targets are often characterized by this type of mechanism.

The false alarms still present in the rooftop of the terminal, indicated by the lower orange rectangle in Figure 2(c), could not be cancelled due to their point-like shape and a significant change in the power of the volume scattering mechanism; i.e. with no additional information these features are similar to cars. Moreover, the side-lobes produced at the bottom edge of the roof of the terminal in Figure 1, had a significant component in the wavelet domain, possibly due to the sparsity of the coefficients provided with the horizontal analysis of the stationary wavelet transform.

Individual cars, in the orange rectangle at the top-left in Figure 2(c), could not be separately identified. The high variability of the appearance of cars when illuminated from different aspect angles, on top of the fact that the side-lobes of close-by targets could merge destructively/constructively are possible reasons for these false alarms.

In contrast to Memmingen, the second site (Oensingen) contained diverse linear structures due to the presence of buildings. Considering the difference of the acquisition geometries and the short term scenario (see Table 1), these linear features induce multiple pairs of false alarms produced by the migration of the PSFs of the walls of the buildings. Here, the curvelet component played a key role in cancelling these errors, while still detecting most real changes on the ground.

However, and due to mathematical limitations, all changes are expressed as a linear combination of their wavelet and curvelet components and thus some errors still remain in the change map, indicated by orange rectangles in Figure 4(c). Additionally, the shapes of these changes are more point-like and therefore attached to the wavelet component, similar to the shape of the changes produced by cars. The migration of the PSFs of some point-like elements on the rooftops was characterized with changes of the power of the even or odd-bounce component (blue and red channels in Figure 3), thus $\wedge CM_{x,wavelet}, \forall\{x\}$ yielded a better solution than $CM_{volume,wavelet}$. The areas influenced by clutter were characterized with a combination of both odd and even-bounce, independently of the shape of the false alarms they induced. The changes produced by the cars could be detected with the wavelet component of any scattering mechanism, and thus $\wedge CM_{x,wavelet}, \forall\{x\}$ did not introduced potential cancelations (mis-detections).

Note that the performance of the method relies on the following assumptions: (1) the scattering regime remains constrant, and (2) the scattering mechanisms of the targets that do not introduce changes are preserved between data sets, even when (slightly) different acquisition geometries exist. Additionally, the performance of the algorithms is constrained by the following limitations: (1) the scattering mechanisms are dependent on the dielectric properties of the targets, the frequency band and the aspect angles, and (2) the ambiguities/incompleteness of the decomposition techniques, which consider the characterization of far-field power measurements (scalars) instead of the 3-D characterization of the electromagnetic field (vectors) [20].

Conclusions

A novel change detector based on MCA was proposed to handle high resolution SAR imagery with a combined local-global noise treatment able to preserve relevant details with well-defined structures. The method's detection performance expedited human interpretation of both the changes and their possible origins. By exploiting the power of the scattering mechanisms and their corresponding shape features, we can significantly improve the performance of the detector for some errors introduced by clutter zones, sidelobes and non-uniform inconsistent geometries. However, the success of the method relies on *a priori* knowledge of the content of the scene (e.g. the possible underlying scattering mechanisms and their feature shapes), and thus some human interaction is still necessary (semi-automatic method).

In future work, we plan to consider a detailed evaluation of the algorithm using spotlighted circular geometries. We are currently analyzing the additional information provided with other polarimetric decompositions and diverse techniques to combine multiple features, and considering the extension to other morphological components. To drive the change detector towards an object-oriented approach, the integration of other image features, such as texture and size is being considered.

REFERENCES

[1] Brunner, D., Lemoine, G. and Bruzzone, L., "Earthquake damage assessment of buildings using VHR optical and SAR imagery," IEEE Transactions on Geoscience and Remote Sensing, 48(5), 2403-2420 (2010).

[2] Schmitt, A., Wessel, B. and Roth, A., "Curvelet approach for SAR image denoising, structure enhancement, and change detection," The International Archives of the Photogrammetry, Remote Sensing and Spatial Information Sciences, 38(3/W4), 151-156 (2009).

[3] Dierking, W. and Skriver, H., "Change detection for thematic mapping by means of airborne multitemporal polarimetric SAR imagery," IEEE Transactions on Geoscience and Remote Sensing, 40(3), 618-636 (2002).

[4] Ranney K.I. and Mehrdad S., "Signal subspace change detection in averaged multilook SAR imagery," IEEE Transactions on Geoscience and Remote Sensing, 44(1), 201-213 (2006).

[5] Conradsen, K., Nielsen, A.A., Schou, J. and Skriver, H., "A test statistic in the complex Wishart distribution and its application to change detection in polarimetric SAR data," IEEE Transactions on Geoscience and Remote Sensing, 41(1), 4-19 (2003).

[6] Kersten, P.R., Lee, J.S. and Ainsworth, T.L., "A comparison of change detection statistics in POLSAR images," Proc. IEEE International Geoscience and Remote Sensing Symposium, 7, 4836-4839 (2005).

[7] Preiss, M. and Stacy Nick, J. S., "Polarimetric SAR Coherent Change Detection," 7th European Conference on Synthetic Aperture Radar EUSAR (Friedrichshafen, Germany), 1-4 (2008).

[8] Molinier, M. and Rauste, Y., "Comparison and evaluation of polarimetric change detection techniques in aerial SAR data," IEEE International Geoscience and Remote Sensing Symposium, 2386-2389 (2007).

[9] Schmitt, A. and Wessel, B., "Introducing Partial Polarimetric Layers into a Curvelet-based Change Detection," 8th European Conference on Synthetic Aperture Radar EUSAR (Aachen, Germany), 1-4 (2010).

[10] Reigber, A., Scheiber, R., Jager, M., Prats-Iraola, P., Hajnsek, I., Jagdhuber, T., Papathanassiou, K.P., Nannini, M., Aguilera, E., Baumgartner, S., Horn, R., Nottensteiner, A. and Moreira, A., "Very-High-Resolution Airborne Synthetic Aperture Radar Imaging: Signal Processing and Applications," Proc. IEEE, 101(3), 759-783 (2013).

[11] Inglada, J., Muron, V., Pichard, D. and Feuvrier, T., "Analysis of Artifacts in Subpixel Remote Sensing Image Registration," IEEE Transactions on Geoscience and Remote Sensing, 45(1), 254-264 (2007).

[12] Freeman, A., "SAR calibration: an overview," IEEE Transactions on Geoscience and Remote Sensing, 30(6), 1107-1121 (1992).

[13] Ainsworth, T.L., Ferro-Famil, L. and Jong-Sen, L., "Orientation angle preserving a posteriori polarimetric SAR calibration," IEEE Transactions on Geoscience and Remote Sensing, 44(4), 994-1003 (2006).

[14] Lee, J. and Pottier, E., [Polarimetric radar imaging: from basics to applications], CRC press, 179-264 (2009).

[15] Dabov, K., Foi, A., Katkovnik, V. and Egiazarian, K., "Image Denoising by Sparse 3-D Transform-Domain Collaborative Filtering," IEEE Transactions on Image Processing, 16(8), 2080-2095 (2007).

[16] Starck, J.-L.; Elad, M. and Donoho, D.L., "Image decomposition via the combination of sparse representations and a variational approach," IEEE Transactions on Image Processing, 14(10), 1570-1582 (2005).

[17] Starck, J.-L., [Sparse Image and Signal Processing: Wavelets, Curvelets and Morphological Diversity], Cambridge University Press, 190-196 (2010).

[18] S. Mallat, [A wavelet tour of signal processing: the sparse way], Elsevier, 2008.
[19] Bobin, J., Starck, J.-L., Fadili, J.M., Moudden, Y. and Donoho, D.L., "Morphological Component Analysis: An Adaptive Thresholding Strategy," IEEE Transactions on Image Processing, 16(11), 2675-2681 (2007).
[20] Sabry R., "A novel field scattering formulation for polarimetric synthetic aperture radar: 3-D scattering and Stokes vector," Progress in Electromagnetics Research (PIER), 57, 129-150 (2012).